Multi-functional Frequency Selective Absorber Enabling FR1 and FR2 5G OTA Tests in a Hybrid Reverberation Chamber

Qingqing Zhang, Zhenzhen Zhao, Junhao Zheng, Furong Li, Jiazhi Tang, and Yi Huang, *Fellow, IEEE*, Yuxin Ren, and Xiaoming Chen, *Senior Member, IEEE*

Abstract—**Due to the special advantages of the reverberation chamber (RC), it has been recognized as a standardized over-the-air (OTA) testing methodology by the cellular telecommunications industry association (CTIA). Currently, OTA tests of the fifth-generation (5G) wireless terminals are usually performed in different testing environments, e.g., in a reverberation chamber for fast isotropic tests in the sub-6 GHz frequency band, and in an anechoic chamber for directional tests in the millimeter-wave (mm-wave) frequency band, which are inconvenient and costly. In this work, two multi-functional frequency selective absorbers (FSAs) are designed to realize absorption in the 5G mm-wave band and reflection/transmission in the sub-6 GHz band. By loading the FSAs to the RC, an integrated testing environment for 5G terminals can be established. Namely, a quasi-anechoic environment in the mm-wave band and a reverberation environment in the sub-6 GHz band can be simultaneously achieved in the RC loaded with the proposed FSAs. Experimental and simulated results are presented to demonstrate the effectiveness of the proposed scheme.**

Index Terms—**Frequency selective absorber (FSA), over-the-air (OTA) testing, reverberation chamber (RC).**

I. INTRODUCTION

WITH the fifth-generation (5G) wireless communication systems established globally, over-the-air (OTA) tests of 5G terminals are attaining increasing attention from both academia and industry, since OTA testing is vital for evaluating the radio performance of wireless devices. Recently, much research has been devoted to the OTA testing for 5G terminals, and the challenges that appeared in 5G OTA tests are discussed in [1]-[3].

Since the 5G spectrum contains the sub-6 GHz band, i.e., frequency range (FR) 1 band, and the millimeter-wave (mm-wave) band, i.e., FR2 band, OTA tests for 5G devices should cover both FR1 and FR2 bands, which causes new challenges for OTA testing. One of the main reasons is that propagation characteristics of the wireless channel are drastically different in the FR1 and FR2 bands. The FR1 channel usually exists a rich multipath effect, whereas the FR2 channel becomes sparse and with much heavier path loss [4]-[6]. The reverberation chamber (RC) is a large metal cavity that (when mode-stirred) can be used to emulate rich multipath environments [7]-[12], making it an efficient testing solution for total radiated power (TRP) and total isotropic sensitivity (TIS) tests in the FR1 band [7], as a cost-effective alternative to the expensive multi-probe anechoic chamber (MPAC) [13], [14]. (For instance, the cost of the RC is about one-third of that of the MPAC in our laboratory.) Unlike sub-6 GHz communications where the terminals are usually equipped with quasi-isotropic antennas, directional array antennas are often used in the mm-wave band to overcome the increased path loss. As a result, directional performance metrics in a non-isotropic environment are of more relevance, making the multi-probe anechoic chamber [2] a more viable testing environment in the FR2 band. For mm-wave channel emulations, however, the MPAC-based OTA testing system with channel emulator has a much higher cost [15], [16]. To reduce the system cost, several paraboloid collimators are used to replace the expensive channel emulator for mm-wave multipath channel emulation [17]. Since the paraboloid collimators require a costly manufacturing process, a hybrid RC where part of the sidewalls is covered with absorbing materials was proposed in [18] to further reduce the system cost. Unfortunately, although this method can partially control the power angular spectrum (PAS) of the mm-wave channel (with the help of a turn-table platform), it will inevitably increase the anisotropy of the sub-6 GHz channel and, therefore, degrade the measurement accuracy of the conventional RC-based OTA test in the FR1 band [8]. Thus, a cost-effective OTA testing solution for both FR1 and FR2 bands is highly desirable. To achieve the desired FR1/FR2 integrated OTA testing environment in the RC, a feasible solution is to use the multifunctional frequency selective surface (FSS). So far the FSS has been extensively investigated for various applications, such as radar cross-

Q. Zhang, J. Zheng, F. Li, J. Tang, and X. Chen are with the School of Information and Communications Engineering, Xi'an Jiaotong University, Xi'an 710049, China (email: xiaoming.chen@mail.xjtu.edu.cn).

Z. Zhao is with College of Information and Computer, Taiyuan University of Technology, Taiyuan 030024, China.

Y. Huang is with the Department of Electrical Engineering and Electronics, University of Liverpool, Liverpool L69 3GJ, UK (e-mail: Yi.Huang@liverpool.ac.uk).

Y. Ren is with China Academy of Information and Communications Technology, Beijing, 100191, China (e-mail: renyuxin@caict.ac.cn).

section (RCS) reduction [19], [20], spatial filters [21], and stealth applications [22].

In this paper, it is shown that, by loading the RC with judiciously designed multi-functional FSS, a cost-effective testing system supporting both FR1 and FR2 OTA tests can be realized. Specifically, the multi-functional FSS should exhibit transmission/reflection properties in the FR1 band and serves as an absorber in the FR2 band. Thus, the desired multifunction FSS can also be referred to as a frequency selective absorber (FSA), which will be used hereafter. The RC loaded with the FSA (i.e., hybrid RC) can functions as a conventional RC in the FR1 band, providing efficient TRP and TIS tests; meanwhile, it offers the possibility of PAS control (with the help of a turntable platform) for directional OTA tests in the FR2 band.

Thus, the main focus of this work is to design the FSA, enabling FR1/FR2 OTA tests in a hybrid RC. Accordingly, a transmissive FSA and a reflective FSA are designed in this work. Both FSAs have a wide absorbing band in the mm-wave band and possess transmission/reflection property in the sub-6 GHz band. (Note that since the FSA is supposed to be attached to the sidewall inside the RC, the transmitted wave will be reflected by the metallic wall. Hence, the transmission and reflection properties of the FSA are equivalent for our purpose.) According to the previous literature, several methods can be used to realize broadband absorption, such as multiple resonances [23]-[25], multilayer structures [26], [27], lumped resistor elements [28], impedance films [29], [30], and three-dimensional structures [31]. In this work, the designed transmissive FSA is loaded with lumped resistors to achieve absorption covering mm-wave band, whereas the design of the reflective FSA is based on impedance films, avoiding the cumbersome soldering of lumped resistors. The reflective FSA is manufactured and tested for experimental validation due to its easy fabrication.

The rest of this paper is organized as follows: Section II gives the detailed design and analysis of the transmissive FSA. Next, the design and analysis of the reflective FSA are presented in Section III. Section IV describes the fabrication and experimental measurements of the reflective FSA. Finally, Section V gives the main conclusions.

II. TRANSMISSIVE FSA BASED ON ASYMMETRIC SPLIT RING SLOTS

A. Element Design

The proposed transmissive FSA structure can be regarded as a combination of an absorptive layer, a bandpass FSS, and a supporting honeycomb in between, as shown in Fig. 1(a). The absorptive layer comprises metallic structures and a thin substrate layer with a thickness of $ha = 0.025$ mm. Fig. 1(b) shows the top view of the absorptive layer, where four identical asymmetric split ring slots (ASRSs) are arranged in fourfold rotational (C4) symmetry (which means rotation by 90° does not change the structure), and loaded with 8 resistors. The black block represents resistors with resistance value $R_a = 360$ Ω. The substrate denoted in blue is Polyimide film, with a relative dielectric constant of $\varepsilon_r = 3.0$ and a loss tangent $\delta = 0.003$. The mediate honeycomb has a thickness of $hs = 1.9$ mm, $\varepsilon_r = 1.07$,

and $\delta = 0.0017$. The bandpass FSS element is composed of three metallic layers separated by two substrate layers. The first and third metallic layers are identical square patches with a gap of $t = 0.7$ mm, as shown in Fig. 1(c). The second layer in the bandpass FSS element is a square ring with a width of $w = 0.6$ mm as shown in Fig. 1(d). Both substrate layers of the bandpass FSS are Rogers RT5880 with a thickness of $ht = 0.3$ mm, $\varepsilon_r = 2.2$, and $\delta = 0.0025$. The parameter values of the FSA structure are shown in Table I.
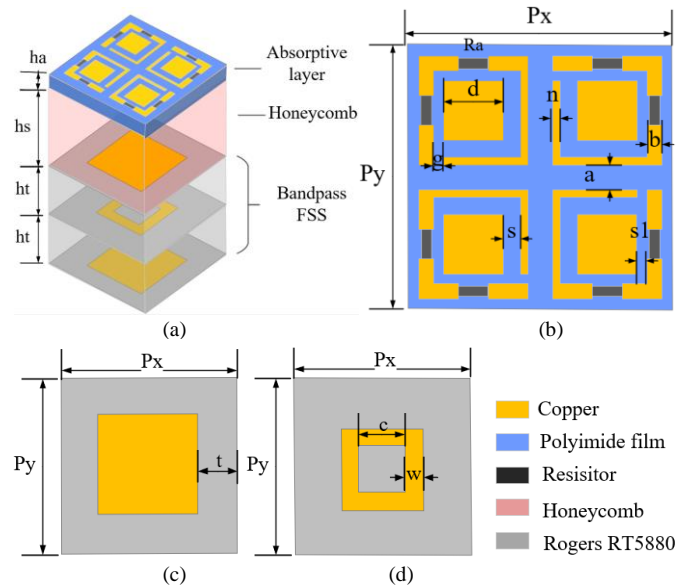

Fig. 1. Geometry of the proposed FSA. (a) Perspective view. (b) Top view. (c) First/third layer and (d) second layer from the bottom.

TABLE I
VARIABLE VALUES OF THE TRANSMISSIVE FSA

Symbol	Px	Py	ha	hs	ht	d	a	g
Value (mm)	5.4	5.4	0.025	1.9	0.3	1.2	0.5	0.2
Symbol	s	s1	n	b	t	w	c	
Value (mm)	0.35	0.2	0.15	0.3	0.9	0.3	0.8	

The proposed FSA is composed of a bandpass FSS and an absorptive layer to achieve a wide passband covering FR1 and an absorption band in FR2, respectively. The bandpass FSS provides a wide passband in the sub-6 GHz band. In the mm-wave band, two absorptive poles are generated by the absorption layer to form a flat absorption band and the FSS serves as a metal ground to avoid transmission, contributing to high absorption to some extent.

B. Equivalent Circuit Model

According to the geometry patterns of the FSA element, the equivalent circuit model (ECM) is presented for further analysis. Generally, the metallic structure in the element can be modeled as equivalent inductance and capacitance. Meanwhile, the substrates can be seen as transmission lines with specific characteristic impedances. The ECM of the transmissive FSA can be seen in Fig. 2.
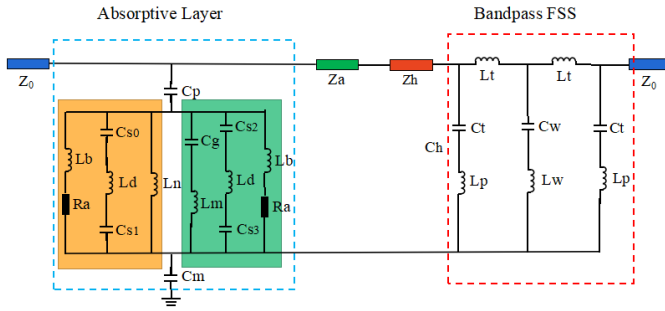
Fig. 2. Equivalent circuit model of the proposed FSA.

As shown in Fig. 2, the ECM of the metallic structure in the absorptive layer can be expressed as the blue dotted box, and the ECM of the bandpass FSS can be expressed as the red dotted box. The transmission lines with specific characteristic impedances Z_a and Z_h represent the thin substrate of the absorptive layer and the honeycomb, respectively. Z_0 is defined as the free-space wave impedance.

In the blue dotted box, the circuit marked by the brown region represents the ECM of the ASRS in the upper left corner, while the green region demonstrates the ECM of the ASRS in the upper right corner. Note that when the FSA is illuminated at normal incidence, the metallic structure parallel with the electric field plays a major role. Thus, it is reasonable to pay attention to the structure with the same orientation as the electric field (the orientation of the electric field is assumed to be vertical here), which leads to identical ECM for the upper and lower ASRSs. So, the corresponding ECM can be simplified into two parts marked by the brown and green regions as mentioned above. C_p represents the gap capacitance between adjacent elements, while C_m represents the capacitance caused by the internal gap between the two upper ASRSs and the two lower ASRSs.

In the meantime, the bandpass FSS can be modeled as the ECM marked by the red dotted box. The substrates of the bandpass FSS are represented by the transmission lines with a specific characteristic impedance which is translated into series inductance and parallel capacitance in the ECM. According to the ECM in Fig. 2, the frequency dependent electromagnetic response of the FSA can be analyzed through the transmission line theory [32]. The impedance of the metallic layer of the absorptive structure can be given by

$$Z_{ap}(\omega) = \frac{1}{j\omega C_P} + \frac{1}{Y_{ASRS}} + \frac{1}{j\omega C_m} \quad (1)$$

where Y_{ASRS} represents the total admittance of the circuits in the brown and green regions (in Fig. 2), and can be written as:

$$Y_{ASRS}(\omega) = \sum_{i=1}^{6} Y_i(\omega). \quad (2)$$

Herein,

$$\begin{cases} Y_1(\omega) = Y_6(\omega) = \dfrac{1}{j\omega L_b + R_a} \\[2mm] Y_2(\omega) = \dfrac{1}{1/j\omega C_{s0} + j\omega L_d + 1/j\omega C_{s1}} \\[2mm] Y_3(\omega) = \dfrac{1}{j\omega L_n} \\[2mm] Y_4(\omega) = \dfrac{1}{1/j\omega C_g + j\omega L_m} \\[2mm] Y_5(\omega) = \dfrac{1}{1/j\omega C_{s2} + j\omega L_d + 1/j\omega C_{s3}} \end{cases} \quad (3)$$

According to the above formulas, the transfer matrix of the circuit marked by blue box can be derived as

$$T_{ap} = \begin{pmatrix} 1 & 0 \\ 1/Z_{ap} & 1 \end{pmatrix}. \quad (4)$$

Furthermore, the transfer matrix of the cascade connection of multiple two-port networks is equal to the product of the transfer matrices of the individual two-port networks [33]. The total transfer matrix of the substrate of the absorptive layer and honeycomb can be expressed as

$$T_s = \begin{pmatrix} \cos\theta_a & jZ_a \sin\theta_a \\ \dfrac{j\sin\theta_a}{Z_a} & \cos\theta_a \end{pmatrix} \begin{pmatrix} \cos\theta_h & jZ_h \sin\theta_h \\ \dfrac{j\sin\theta_h}{Z_h} & \cos\theta_h \end{pmatrix} \quad (5)$$

where θ_a and θ_h are the phases corresponding to the phase constants and the lengths of the equivalent transmission lines, respectively. Next, the transfer matrix of the bandpass FSS can be calculated as

$$T_{FSS} = \prod_{i=1}^{5} T_i \quad (6)$$

where

$$\begin{cases} T_1 = T_5 = \begin{pmatrix} 1 & 0 \\ \dfrac{1}{1/j\omega C_t + j\omega L_p} & 1 \end{pmatrix} \\[4mm] T_2 = T_4 = \begin{pmatrix} 1 & j\omega L_t \\ 0 & 1 \end{pmatrix} \\[4mm] T_3 = \begin{pmatrix} 1 & 0 \\ \dfrac{1}{j\omega L_w + 1/j\omega C_w} & 1 \end{pmatrix} \end{cases} \quad (7)$$

The total transfer matrix of the FSA can be written as

$$T_{FSA} = \begin{pmatrix} A & B \\ C & D \end{pmatrix} = T_{ap} T_s T_{FSS}. \quad (8)$$

Thus, the reflection coefficient S_{11}, transmission coefficient S_{21}, and absorption A_{FSA} of the FSA can be derived from the transfer matrix according to [34]

$$S_{11} = \frac{A + B/Z_0 - CZ_0 - D}{A + B/Z_0 + CZ_0 + D}, \tag{9}$$

$$S_{21} = \frac{2}{A + B/Z_0 + CZ_0 + D}, \tag{10}$$

$$A_{FSA} = 1 - |S_{11}|^2 - |S_{21}|^2. \tag{11}$$

The ECM provided a simple method to analyze the structure of the FSA. For instance, the ECM was first employed to develop an initial design of the FSS in [35] and the values of the lumped components were then obtained by matching the frequency responses of full-wave simulation results. A reliable procedure to calculate the values of the lumped components is described in [36]. For a single lossless resonate LC circuit, the impedance of the circuit can be written as

$$Z(\omega) = \frac{1}{j\omega C} + j\omega L. \tag{12}$$

By imposing the impedance values at two frequency points, the values of L and C can be calculated respectively as

$$C = \frac{\omega_1 - \omega_2^2/\omega_1}{-j\omega_2^2 Z(\omega_1) + j\omega_1\omega_2 Z(\omega_2)}, \tag{13}$$

$$L = \frac{-jZ(\omega_1) + 1/\omega_1 C}{\omega_1}. \tag{14}$$

TABLE II
VARIABLE VALUES OF THE EQUIVALENT CIRCUIT MODEL

Symbol	L_t	C_{s1}	C_{s0}	L_d	L_b	L_n
Value	0.90 nH	0.02 pF	0.43 pF	0.49 nH	0.13 nH	0.58 nH
Symbol	L_m	C_{s2}	L_d	C_{s3}	C_m	C_g
Value	1.00 nH	0.01 pF	0.49 nH	0.09 pF	0.06 pF	0.10 fF
Symbol	C_w	C_t	L_w	L_p	C_p	
Value	0.10 fF	0.02 pF	2.95 nH	1.05 nH	0.04 pF	

$Z(\omega_1)$ and $Z(\omega_2)$ are the impedance values at two frequency points obtained by full-wave simulations. The relationship between variable values and the electromagnetic response of the FSA has been obtained by (1) - (11). Thus, the initial values of the circuit parameters can be estimated by imposing several points of the frequency response. (Note that by imposing the resonant points, more reliable results can be obtained.) Due to the large number of parameters presented in the ECM, the calculation process is complex, so only the scopes of the parameter values are estimated based on the resonant points of the frequency response and the geometrical dimensions of the FSA structure. Then iterative optimization procedure is performed using Advanced Design System (ADS) software, and the optimized values of the circuit parameters are shown in Table II. It is obvious that the reflection coefficient and transmission coefficient of the equivalent two-port network depend on the values of the element parameters, and the

parameters are corresponding to the geometrical dimensions of the FSA. Once the circuit model of the proposed FSA is obtained, the existing circuit optimizer can be used to shape the electromagnetic response and the corresponding geometrical parameters can be optimized to satisfy the given objective. The circuit model can predict the electromagnetic behavior of the FSA and helps in the design process of the FSA structures.
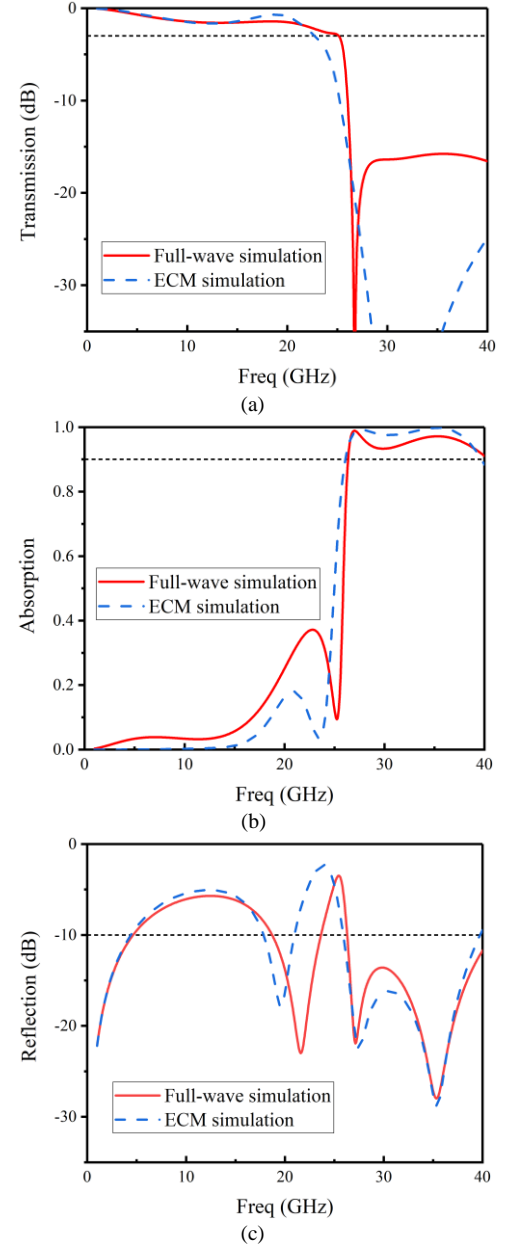

(a)

(b)

(c)

Fig. 3. Full-wave and ECM simulation results of the proposed transmissive FSA. (a) Transmission curves. (b) Absorption curves. (c) Reflection curves.

C. Performance of the FSA

The full-wave simulation of the FSA is conducted by using CST Microwave Studio and the ECM simulation of the FSA is performed in ADS. The corresponding results are shown in Fig. 3. The transmission coefficients at normal incidence can be seen in Fig. 3(a), where the -3 dB transmission band ranges from 0 to 25 GHz, and the -1 dB transmission band can cover the sub-6 GHz band. The transmission characteristic is realized

by the bandpass FSS below the absorptive layer in the FSA structure. The resonance at 21.9 GHz is mainly generated by square metal patches in the first and third layers (from the bottom) of the FSS. The coupling between the metal layers also contributes to the resonance at 21.9 GHz. Fig. 3(b) demonstrates the absorption performance of the FSA. It can be observed that the absorption band is generated in the mm-wave frequency range. The absorption frequency band (absorption rate > 0.9) ranges from 26 to 40 GHz. The reflection curves of the FSA are presented in Fig. 3(c), where the -10 dB reflection band in the mm-wave band ranges from 26 to 40 GHz.

From the simulated results presented in Fig. 3, it can be seen that the FSA can realize both a wide passband and a flat absorption band with a high absorption rate and a fast roll-off in between. In addition, the response curves of the ECM are comparable to the full-wave simulation results, so the ECM can be used to interpret the FSA properly.

Although the design achieves the desired transmission and absorption performances in the sub-6 GHz and mm-wave bands, respectively, the resisters loaded in the FSA and the multilayer structures bring challenges to the manufacture, and the angular stability is unsatisfactory. In order to satisfy the requirements of RC loading and increase the angular stability, a reflective FSA based on impedance films is proposed in Section III.

III. REFLECTIVE FSA BASED ON IMPEDANCE FILMS

A. Element Design

The reflective FSA is designed based on impedance films in order to achieve a wide absorptive band in the millimeter wave frequency range. The impedance film is made by polyethylene-terephthalate (PET) deposited with indium-tin-oxide (ITO) [30]. Compared with resistors, the impedance films can greatly simplify the fabrication of the FSA and increase the robustness of the designed FSA to e.g., complicated resistor soldering. Moreover, the angular stability of the proposed FSA can also be enhanced.
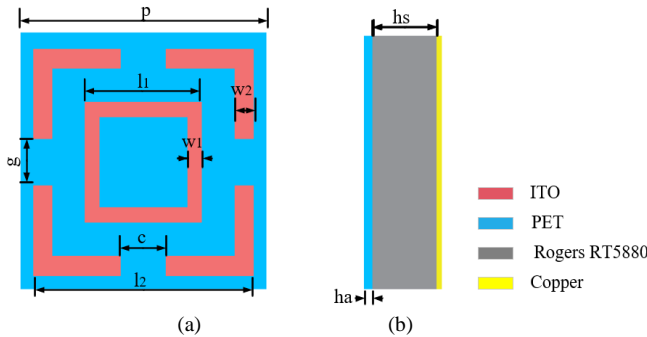

(a)   (b)
Fig. 4. Geometry of the proposed reflective FSA. (a) Top view. (b) Side view.

TABLE III
VARIABLE VALUES OF THE TRANSMISSIVE FSA

Symbol	p	l2	l1	w1	w2	c	g	ha	hs
Value (mm)	5	4.5	2.4	0.3	0.4	0.2	0.2	0.175	1.3

The structure of the proposed reflective FSA is presented in Fig. 4. The impedance film layer is placed on top of the substrate. The ITO with a sheet resistance of 50 Ω/sq is denoted in red color while its supporting structure PET is represented in blue. The ITO structure contains a square ring in the middle and four surrounding L shape patches. The centrosymmetric structure ensures polarization insensitivity. It is noted that the PET has a thickness of 0.175 mm, $\varepsilon_r = 3$, and $\delta = 0.06$. The ITO thickness is almost negligible. The substrate denoted in grey color is Rogers RT5880, with a thickness of 1.3 mm, $\varepsilon_r = 2.2$, and $\delta = 0.001$. The copper ground denoted in yellow color is patched on the back of the substrate. The parameter values of the structure in Fig. 4 are presented in Table III.

In the sub-6 GHz frequency band, the incident wave passes through the top layer and is reflected by the copper ground. Thus, the FSA can present reflective property in the FR1 band. In the mm-wave band, the ITO structures become resonant and the incident wave generates maximal induced current on the surface of the FSA. Therefore, most of the energy of incident waves is absorbed by the FSA.

B. Equivalent Circuit Model

The ECM of the reflective FSA is obtained in this part to understand its working principle. The whole structure of the FSA can be regarded as a two-port network, and the substrates can be seen as transmission lines, which can be modeled by series inductance and parallel capacitance.
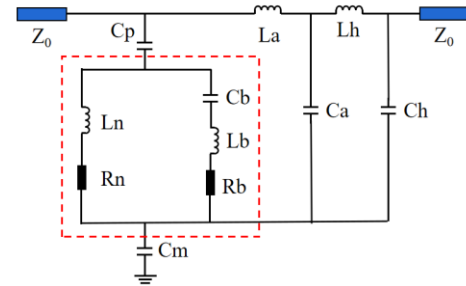

Fig. 5. Equivalent circuit model of the proposed FSA.

Since the ITO has a sheet resistance, the patterns of ITO need to be modeled by equivalent capacitance, inductance, and resistance. The ECM of the FSA is shown in Fig. 5.

C_p is the gap capacitance between FSA elements, and the capacitance caused by the gap between adjacent L-shaped structures is represented by C_m. L_n and R_n represent the inductance and resistance of the L-shaped patch. The inductance and resistance of the square ring located in the middle are equivalent to L_b and R_b, while C_b is the capacitance between the L-shaped structure and the square ring. The PET is equivalent to series L_a and parallel C_a, and the substrate is modeled by L_h and C_h. Z_0 is the free-space wave impedance.

The impedance of the ITO layer can be obtained as

$$Z_r(\omega) = \frac{1}{j\omega C_P} + \frac{1}{Y_L} + \frac{1}{j\omega C_m} \qquad (15)$$

where Y_L is the admittance of the circuit in the red-dotted region in Fig. 5 and can be written as

$$Y_L(\omega) = \frac{1}{j\omega L_n + R_n} + \frac{1}{1/j\omega C_b + j\omega L_b + R_b} . \qquad (16)$$

The transfer matrix of the ITO layer can be presented as

$$T_r = \begin{pmatrix} 1 & 0 \\ 1/Z_r & 1 \end{pmatrix}. \tag{17}$$

In addition, the transfer matrix of the PET and the substrate layer can be expressed as

$$T_s = \begin{pmatrix} 1 & j\omega L_a \\ 0 & 1 \end{pmatrix} \begin{pmatrix} 1 & 0 \\ j\omega C_a & 1 \end{pmatrix} \begin{pmatrix} 1 & j\omega L_h \\ 0 & 1 \end{pmatrix} \begin{pmatrix} 1 & 0 \\ j\omega C_h & 1 \end{pmatrix}. \tag{18}$$

The total transfer matrix of the FSA can then be expressed as

$$T_{FSA} = \begin{pmatrix} A & B \\ C & D \end{pmatrix} = T_r T_s. \tag{19}$$

The reflection coefficient S_{11} can be determined from the transfer matrix as

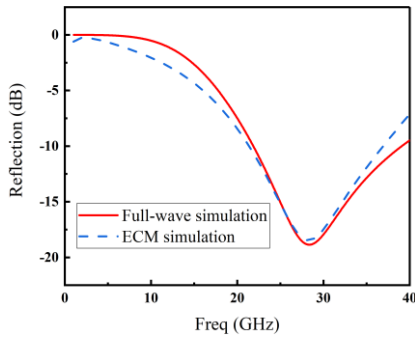$$S_{11} = \frac{A + B/Z_0 - CZ_0 - D}{A + B/Z_0 + CZ_0 + D}. \tag{20}$$

Fig. 6. Full-wave and ECM simulation results of the reflective FSA.

TABLE IV
VARIABLE VALUES OF EQUIVALENT CIRCUIT MODEL

Symbol	C_m	C_p	L_a	L_h	C_a	L_b
Value	4.77 pF	8.00 pF	1.36 nH	3.09 nH	0.01 pF	1.00 nH
Symbol	L_n	R_n	C_b	C_h	R_b	
Value	2.45 nH	5.62 Ω	0.01 pF	0.01 fF	365.20 Ω	

As can be seen from Fig. 6, The reflection coefficient of the FSA obtained from the ECM shows a good agreement with the CST simulation result. The variable values in the ECM of the reflective FSA are determined by the approach described in Section II and presented in Table IV.

C. Performance of the FSA

Owing to the compact symmetric structure and ultrathin thickness, the reflective FSA is polarization-insensitive and has good angular stability. The simulation of the reflective FSA is performed in the full wave simulation software CST, where unit cell boundary conditions were set. By changing the polarizations and incident angles of the incident wave, the absorption performance of the reflective FSA under different waves can be obtained. The performance of the FSA is presented in Fig. 7. In order to verify the angular stability of the FSA, the absorptions of the FSA at different oblique incident angles under TE mode and TM mode are investigated.

Fig. 7 (a) shows the absorption of the FSA at different incident angles under TE mode. It can be seen from the figure that the absorption band of the FSA ranges from 22 GHz to 40 GHz, and the absorption rate is higher than 0.9 within the band. Moreover, the performance of the FSA remains good up to 50° incident angle. Fig. 7 (b) gives the absorption of the FSA at different incident angles under TM mode. It shows that the FSA possesses stable absorptive property in the mm-wave band under both TE and TM modes. In the sub-6 GHz band, the absorption of the FSA is approximately equal to zero. Due to the metal layer placed on the back of the FSA, the transmission coefficient of the FSA is negligible. So, almost all the wave can be reflected by the FSA within the FR1 band.
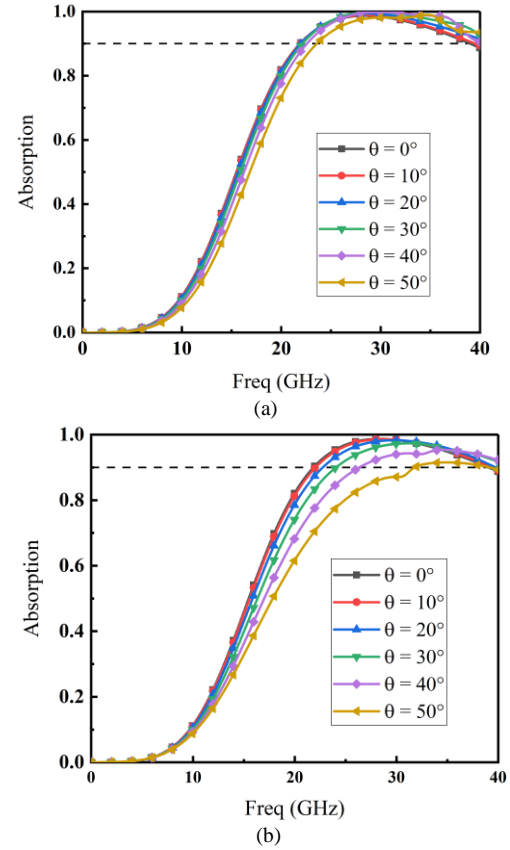

(a)

(b)

Fig. 7. Reflection coefficients of the proposed reflective FSA under different polarizations and incident angles. (a) TE mode. (b) TM mode.

IV. EXPERIMENTAL VERIFICATION

Both the transmissive and reflective FSAs designed in Section II and Section III satisfy the requirements for FR1/FR2 hybrid RC loading. Nevertheless, for proof of concept and easy fabrication, only the reflective FSA is chosen for manufacturing.

The reflective FSA prototype is composed of 80 × 80 unit cells, with an overall size of 400 mm × 400 mm. A photograph of the prototype is shown in Fig. 8(a). The measurement setup for reflection coefficients in the laboratory is illustrated in Fig. 8(b). The transmitting antenna and receiving antenna are mounted on two mechanical arms and connected to a vector network analyzer through coaxial cables. Three pairs of dual-polarized horn antennas are used in order to cover the whole

testing band. The reflective FSA is placed in the center and surrounded by absorbing materials to reduce diffraction from the environment. The distance from the horn antennas to the reflective FSA is 1.5 m. A metal plate of the same size as the FSA is used for calibration. By controlling the rotation angles of the mechanical arms, the reflection coefficients of the reflective FSA under different incident angles are obtained. In addition, the reflection coefficients of the FSA under different polarizations are gathered by rotating the transmitting and receiving antennas.
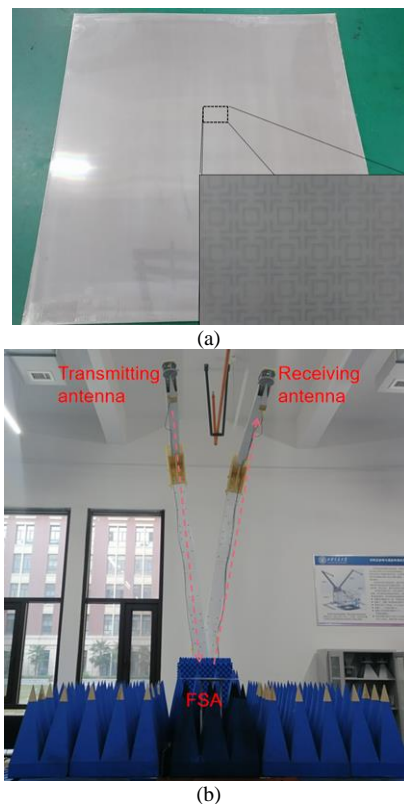

(a)

(b)

Fig. 8. Fabrication and measurements of the proposed FSA. (a) A prototype consisting of 80 $\times$ 80 units. (b) Measurements setup in the laboratory.

Finally, the measured reflection coefficients of the FSA at different oblique incident angles under TM and TE polarizations are presented in Fig. 9 (a) and Fig. 9 (b), respectively. The simulated result at a normal incident angle is also presented in the figure for better comparison. From the figure, it can be seen that the fractional bandwidth of the FSA under -10 dB is about 58% at the normal incident, and the performance of the FSA is stable within 50° for both TE and TM polarizations. Moreover, a reasonable agreement is observed between the simulated and measured results. The discrepancies between the two results are mainly caused by the diffraction from the testing environment (see Fig. 8) and errors in manufacturing. (The testing environment and calibration has been discussed in [37]. Note that the film layer and the PCB layer of the prototype has been manufactured separately, which have to be added together via optically clear adhesive glue. This post-process must be carefully performed to eliminate any possible air gap in between to ensure good performance.)

In addition to the reflection measurements, the FSA's performance in a real RC is tested. The measurement environment of the RC loaded with four pieces of FSA is shown in Fig. 10, where the FSA is mounted on the RC side walls. The transmitting antenna is mounted on the rotating platform and rotates 360° with an azimuthal interval of 3°, and the receiving antenna is placed at a corner of the loaded RC. The testing frequency is divided into two ranges of 1-6 GHz and 26-40 GHz, and 1001 frequency points are chosen for each of the frequency ranges. In this work, the distance between the center of the transmission antenna and the rotating platform is defined as the rotating radius, and the synthetic aperture method [38] is used to obtain the power angular spectra under different rotating radii to better illustrate the power attenuation influenced by the FSA. Three different rotating radii of 24 cm, 13 cm, and 2 cm are chosen. Then, S_{21} is sampled in the loaded RC and the results are processed and shown in Figs. 11 and 12.
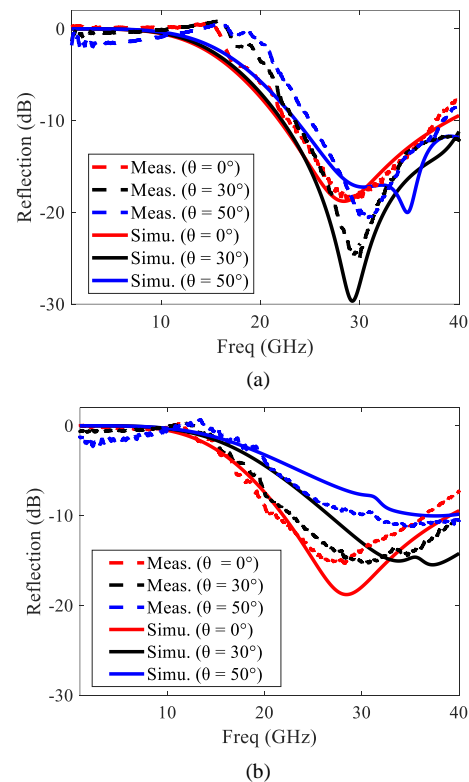

(a)

(b)

Fig. 9. Experimental results under different polarizations and incident angels. (a) TE mode. (b) TM mode.
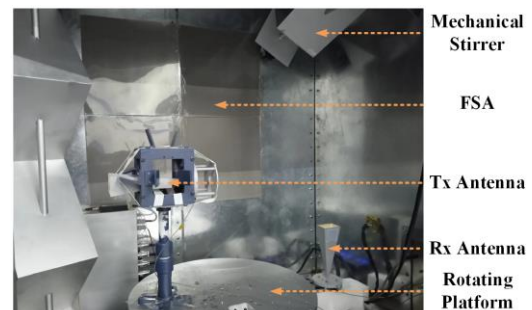

Fig. 10. Measurement setup in the loaded RC.

S_{21} for the frequency range of 1-6 GHz under the rotating radius of 24 cm with three mechanical stirrings was measured, and the power-angle-frequency spectrum is shown in Fig. 11 (a). The power-angle-delay spectrum can then be acquired by using the Fourier transformation, shown in Fig. 11 (b). It can be known from the results that the FSA does not absorb power in the frequency range of 1-6 GHz. Thus, the FSA-loaded hybrid RC behaves like the traditional RC allowing efficient TRP and TIS tests in the FR1 band.
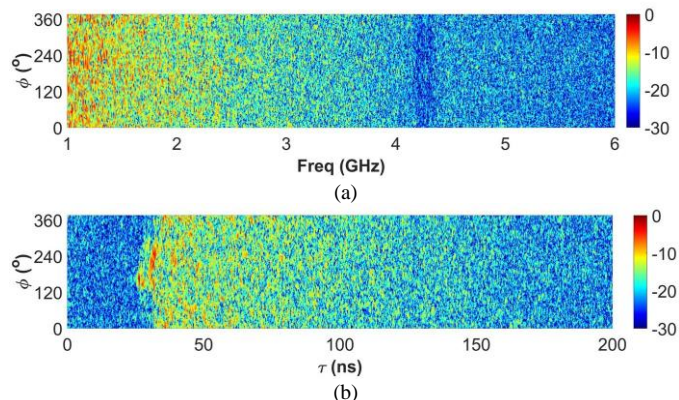

Fig. 11. Average (a) power-angle-frequency and (b) power-angle-delay spectra of the sub-6 GHz channel with a radius and three mechanical stirrings.
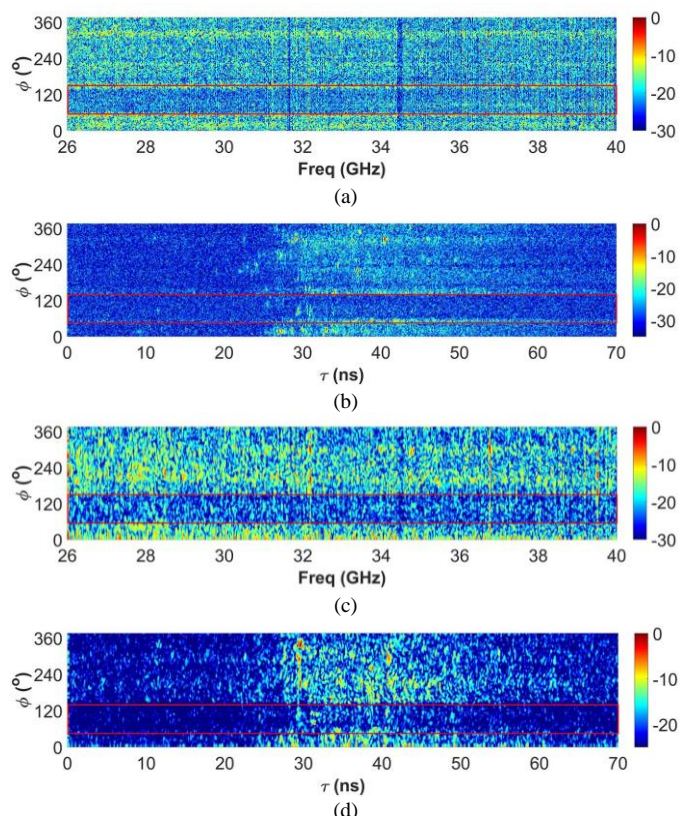

Fig. 12. Average (a) power-angle-frequency and (b) power-angle-delay spectra with a radius and three mechanical stirrings, and average (c) power-angle-frequency and (d) power-angle-delay spectra for the synthetic aperture method with three radii and three mechanical stirrings, all in the mm-wave range.

To further illustrate the absorbing characteristic of the designed FSA, S_{21} in the frequency range of 26 - 40 GHz is measured. The two-dimensional power-angle-frequency spectra with multi-frequency points can be obtained, as shown in Figs. 12(a) and (c). The power spectrum using a radius and three mechanical stirrings is shown in Fig. 12(a), whereas the power spectrum of the synthetic aperture result using all three radii and mechanical stirrings is presented in Fig. 12(c). Note that the angular range of the red box in the figures corresponds to the angular coverage of the FSA, i.e., (60°, 120°). The synthetic aperture method is supposed to yield a more accurate estimation of the power angular spectrum.

The power-angle-delay spectra in the time domain can then be obtained by using the Fourier transformation, as shown in Figs. 12 (b) and (d), whereas the power attenuations are also marked by the red box. Comparing the results of Figs. 11 and 12, it is safe to conclude that the spectral powers in the directions covered by the FSA are significantly attenuated in the FR2 band, whereas the FSA has no effect on the angular spectrum in the FR1 band. Hence, the effectiveness of the designed FSA is well proved. Namely, the FSA-loaded hybrid RC provides an efficient way to control the PAS of the mm-wave channel (enabling directional OTA tests in the FR2 band) and has little influence on the isotropy of the sub-6 GHz channel (ensuring efficient TRP and TIS tests in the FR1 band).

V. CONCLUSIONS

In this article, an integrated OTA testing environment for 5G terminals has been proposed by loading the RC with a specially designed FSA. Two types of multifunctional FSAs have been designed to support this scheme. Both of the FSAs could offer high absorption from 26 GHz to 40 GHz while exhibiting transmissive/reflective property in the sub-6 GHz frequency band. For easy fabrication, the reflective FSA with ITO (instead of lumped resistors) was chosen for experimental verification. Several measurements have been conducted to validate the performance of the proposed FSA, including reflective coefficients, angular stability, and polarization insensitivity. The measurement results showed reasonable agreement with the simulations. Besides, further experiments have been performed in the RC with FSAs attached on a sidewall to show that the resulting hybrid RC could realize an integrated FR1/FR2 OTA testing environment for 5G terminals. It was experimentally validated that, by loading the RC with the proposed FSA, directional OTA tests in the FR2 band could be enabled, while efficient TRP/TIS tests could still be kept in the FR1 band, providing a cost-effective OTA testing solution for both FR1 and FR2 bands.

REFERENCES

[1] Y. Qi *et al.*, "5G over-the-air measurement challenges: Overview," *IEEE Trans. Electromagn. Compat.*, vol. 59, no. 6, pp. 1661-1670, Dec. 2017.

[2] H. Pei *et al.*, "Key issues and algorithms of multiple-input-multiple-output over-the-air testing in the multi-probe anechoic chamber setup," *Sci. China Inf. Sci.*, vol. 65, no. 3, 2022, Art. no. 131302, doi: 10.1007/s11432-021-3285-y.

[3] P. Zhang, X. Yang, J. Chen and Y. Huang, "A survey of testing for 5G: Solutions, opportunities, and challenges," *China Commun.*, vol. 16, no. 1, pp. 69-85, Jan. 2019.

[4] P. Kildal and A. A. Glazunov, "OTA testing of 3G-5G devices with MIMO: From anechoic chambers to reverberation chambers and back

again?" in *Proc. IEEE Int. Symp. Antennas Propag. USNC/URSI Nat. Radio Sci. Meeting*, 2017, pp. 1697-1698.

[5] K. Guan, B. Ai, B. Peng, *et al.*, "Towards Realistic High-Speed Train Channels at 5G Millimeter-Wave Band – Part I: Paradigm, Significance Analysis, and Scenario Reconstruction," *IEEE Trans. Veh. Technol.*, vol. 67, no. 10, pp. 9112 – 9128, Oct. 2018.

[6] R. He, B. Ai, G. Wang, *et al.*, "Wireless channel sparsity: measurement, analysis, and exploitation in estimation," *IEEE Wireless Commun.*, vol. 28, no. 4, pp. 113-119, Aug. 2021.

[7] W. Xue, F. Li, X. Chen, S. Zhu, A. Zhang and T. Svensson, "A unified approach for uncertainty analyses for total radiated power and total isotropic sensitivity measurements in reverberation chamber," *IEEE Trans. Instrum. Meas.*, vol. 70, 2021, Art. no. 1003112, doi: 10.1109/TIM.2020.3041079.

[8] P. -S. Kildal, X. Chen, C. Orlenius, M. Franzen and C. S. L. Patane, "Characterization of reverberation chambers for OTA measurements of wireless devices: Physical formulations of channel matrix and new uncertainty formula," *IEEE Trans. Antennas Propag.*, vol. 60, no. 8, pp. 3875-3891, Aug. 2012.

[9] V. Rajamani, C. F. Bunting, J. C. West, "Stirred-mode operation of reverberation chambers for EMC testing," *IEEE Trans. Instrum. Meas.*, vol. 61, no. 10, pp. 2759-2764, Oct. 2012.

[10] A. Gifuni, L. Bastianelli, F. Moglie, V. M. Primiani and G. Gradoni, "Base-Case Model for Measurement Uncertainty in a Reverberation Chamber Including Frequency Stirring," *IEEE Trans. Electromagn. Compat.*, vol. 60, no. 6, pp. 1695-1703, Dec. 2018.

[11] V. M. Primiani et al., "Reverberation chambers for testing wireless devices and systems," *IEEE Electromagn. Compat. Mag.*, vol. 9, no. 2, pp. 45-55, 2020.

[12] K. A. Remley, C. -M. J. Wang, D. F. Williams, J. J. aan den Toorn, and C. L. Holloway, "A significance test for reverberation-chamber measurement uncertainty in total radiated power of wireless devices," *IEEE Trans. Electromagn. Compat.*, vol. 58, no. 1, pp. 207-219, Feb. 2016.

[13] S. Huang, F. Li, and X. Chen, "An improved method for total radiated power tests in anechoic chambers," *IEEE Trans. Instrum. Meas.*, vol. 71, 2022, Art. no. 1005909, doi: 10.1109/TIM.2022.3197763.

[14] J. Li, Y. Qi, W. Yu, *et al.*, "Total isotropic sensitivity measurement in switched beam antenna systems," *IEEE Trans. Instrum. Meas.*, vol. 69, no. 8, pp. 5458–5467, Aug. 2020, doi: 10.1109/TIM.2019.2958472.

[15] P. Kyösti, L. Hentilä, W. Fan, J. Lehtomäki and M. Latva-Aho, "On radiated performance evaluation of massive MIMO devices in multiprobe anechoic chamber OTA setups," *IEEE Trans. Antennas Propag.*, vol. 66, no. 10, pp. 5485-5497, Oct. 2018.

[16] Y. Li, L. Xin, X. Liu and X. Zhang, "Dual anechoic chamber setup for over-the-air radiated testing of 5G devices," *IEEE Trans. Antennas Propag.*, vol. 68, no. 3, pp. 2469-2474, Mar. 2020.

[17] C. Rowell, B. Derat, and A. Cardalda-García, "Multiple CATR reflector system for multiple angles of arrival measurements of 5G millimeter wave devices," *IEEE Access*, vol. 8, pp. 211324-211334, 2020.

[18] M. G. Becker, R. D. Horansky, D. Senic, V. Neylon and K. A. Remley, "Spatial channels for wireless over-the-air measurements in reverberation chambers," in *Proc. 12th Eur. Conf. Antennas Propag. (EUCAP)*, Apr. 2018, pp. 1–5.

[19] Z. Huang *et al.*, "Partition layout loading of frequency selective surface absorbers on the curved surfaces for the significant RCS reduction," *IEEE Trans. Microw. Theory Techn.*, vol. 70, no. 6, pp. 2948-2954, June 2022.

[20] W. Wu, X. Liu, K. Cui, Y. Ma and Y. Yuan, "An ultrathin and polarization-insensitive frequency selective surface at Ka-band," *IEEE Antennas Wireless Propag. Lett.*, vol. 17, no. 1, pp. 74-77, Jan. 2018.

[21] A. Lalbakhsh, M. U. Afzal, K. P. Esselle and S. L. Smith, "All-metal wideband frequency-selective surface bandpass filter for TE and TM polarizations," *IEEE Trans. Antennas Propag.*, vol. 70, no. 4, pp. 2790-2800, Apr. 2022.

[22] V. K. Chakradhary, H. B. Baskey, R. Roshan, A. Pathik and M. J. Akhtar, "Design of frequency selective surface-based hybrid nanocomposite absorber for stealth applications", *IEEE Trans. Microw. Theory Techn.*, vol. 66, no. 11, pp. 4737-4744, Nov. 2018.

[23] M. Li, S. Xiao, Y. -Y. Bai and B. -Z. Wang, "An ultrathin and broadband radar absorber using resistive FSS," *IEEE Antennas Wireless Propag. Lett.*, vol. 11, pp. 748-751, 2012.

[24] Z. Yao, S. Xiao, Z. Jiang, L. Yan and B. -Z. Wang, "On the design of ultrawideband circuit analog absorber based on quasi-single-layer FSS," *IEEE Antennas Wireless Propag. Lett.*, vol. 19, no. 4, pp. 591-595, Apr. 2020.

[25] A. A. Omar and Z. Shen, "Tunable absorptive frequency-selective transmission structure," in *Proc. IEEE Int. Symp. Antennas Propag. USNC/URSI Nat. Radio Sci. Meeting*, 2018, pp. 2063-2064.

[26] S. Ghosh and K. V. Srivastava, "A polarization-independent broadband multilayer switchable absorber using active frequency selective surface," *IEEE Antennas Wireless Propag. Lett.*, vol. 16, pp. 3147-3150, 2017.

[27] Y. Tayde, M. Saikia, K. V. Srivastava and S. A. Ramakrishna, "Polarization-insensitive broadband multilayered absorber using screen printed patterns of resistive ink," *IEEE Antennas Wireless Propag. Lett.*, vol. 17, no. 12, pp. 2489-2493, Dec. 2018.

[28] A. Parameswaran, A. A. Ovhal, D. Kundu, H. S. Sonalikar, J. Singh and D. Singh, "A low-profile ultra-wideband absorber using lumped resistor-loaded cross dipoles with resonant nodes," *IEEE Trans. Electromagn. Compat.*, vol. 64, no. 5, pp. 1758-1766, Oct. 2022.

[29] K. Takizawa and O. Hashimoto, "Transparent wave absorber using resistive thin film at V-band frequency," *IEEE Trans. Microw. Theory Techn.*, vol. 47, no. 7, pp. 1137-1141, Jul. 1999.

[30] M. Lin, J. Yi, X. Chen, Z. H. Jiang, L. Zhu, P. Qi, S. N. Burokur. "Compact multi-functional frequency-selective absorber based on customizable impedance films," *Opt. Express*, vol. 29, no. 10, pp. 14974-14984, May 2021.

[31] X. Jiang, A. K. Rashid, W. Xu, Q. Cheng, L. Shao and Q. Zhang, "An ultrawideband three-dimensional bandpass frequency selective surface," *IEEE Antennas Wireless Propag. Lett.*, vol. 21, no. 6, pp. 1238-1242, Jun. 2022.

[32] D. M. Pozar. *Microwave Engineering*, 4th ed. Hoboken, NJ, USA: Wiley, 2012.

[33] Terry C. Edwards, Michael B. Steer, "Microwave network analysis," in *Foundations for Microstrip Circuit Design*, Wiley-IEEE Press, pp.51-75, 2016.

[34] D. A. Frickey, "Conversions between S, Z, Y, H, ABCD, and T parameters which are valid for complex source and load impedances," *IEEE Trans. Micro. Theory Techn.*, vol. 42, no. 2, pp. 205-211, Feb. 1994.

[35] Y. E. Erdemli, K. Sertel, R. A. Gilbert, D. E. Wright and J. L. Volakis, "Frequency-selective surfaces to enhance performance of broad-band reconfigurable arrays," *IEEE Trans. Antennas Propag.*, vol. 50, no. 12, pp. 1716-1724, Dec. 2002.

[36] F. Costa, A. Monorchio and G. Manara, "Efficient analysis of frequency-selective surfaces by a simple equivalent-circuit model," *IEEE Antennas Propag. Mag.*, vol. 54, no. 4, pp. 35-48, Aug. 2012.

[37] J. Yi, C. Dong, W. Xue, and X. Chen, "A switchable metamaterial absorber for fine tuning of the coherence bandwidth in a reverberation chamber," *IEEE Trans. Antennas Propag.*, vol. 70, no. 6, pp. 4908-4913, Jun. 2022.

[38] R. J. Pirkl and K. A. Remley, "Experimental evaluation of the statistical isotropy of a reverberation chamber's plane-wave spectrum," *IEEE Trans. Electromagn. Compat.*, vol. 56, no. 3, pp. 498–509, Jun. 2014.